Portable, handheld, and affordable blood perfusion imager for screening of subsurface cancer in resource-limited settings

Arka Bhowmik[a] , Biswajoy Ghosh[a], Mousumi Pal[b], Ranjan Rashmi Paul[b], Jyotirmoy Chatterjee[a], and Suman Chakraborty[c,1]

[a]School of Medical Science and Technology, Indian Institute of Technology Kharagpur, Kharagpur 721302, India; [b]Department of Oral and Maxillofacial Pathology, Guru Nanak Institute of Dental Science and Research, Kolkata 700114, India; and [c]Department of Mechanical Engineering, Indian Institute of Technology Kharagpur, Kharagpur 721302, India

Precise information on localized variations in blood circulation holds the key for noninvasive diagnostics and therapeutic assessment of various forms of cancer. While thermal imaging by itself may provide significant insights on the combined implications of the relevant physiological parameters, viz. local blood perfusion and metabolic balance due to active tumors as well as the ambient conditions, knowledge of the tissue surface temperature alone may be somewhat inadequate in distinguishing between some ambiguous manifestations of precancer and cancerous lesions, resulting in compromise of the selectivity in detection. This, along with the lack of availability of a user-friendly and inexpensive portable device for thermal-image acquisition, blood perfusion mapping, and data integration acts as a deterrent against the emergence of an inexpensive, contact-free, and accurate in situ screening and diagnostic approach for cancer detection and management. Circumventing these constraints, here we report a portable noninvasive blood perfusion imager augmented with machine learning–based quantitative analytics for screening precancerous and cancerous traits in oral lesions, by probing the localized alterations in microcirculation. With a proven overall sensitivity >96.66% and specificity of 100% as compared to gold-standard biopsy-based tests, the method successfully classified oral cancer and precancer in a resource-limited clinical setting in a double-blinded patient trial and exhibited favorable predictive capabilities considering other complementary modes of medical image analysis as well. The method holds further potential to achieve contrast-free, accurate, and low-cost diagnosis of abnormal microvascular physiology and other clinically vulnerable conditions, when interpreted along with complementary clinically evidenced decision-making perspectives.

cancer screening | resource-limited setting | blood perfusion sensor

Blood perfusion, defined as the volume flow rate of blood through a given extent of a tissue, is a crucial quantitative index, depicting physiological phenomena in the capillary network and extracellular spaces within the tissue matrix and dictating decisive assessments concerning the tissue health and diseases. In practice, measurements of superficial blood perfusion disclose functionally relevant information for a multitude of medical applications, including but not limited to screening of skin lesion (1), assessment of breast cancer treatment protocols (2, 3), tumor-induced vasculature and metastasis (4), effect of antiangiogenic agents (5), diabetically triggered vasodilation disorder (6), viability of a transplanted tissue graft (7), healing of wounds (8) and burns (9), and monitoring of peripheral arterial (10) and obstructive coronary arterial diseases (11). Quantitative estimates of blood perfusion are intrinsically fundamental to the tissue and tumor metabolism (12, 13). Such data may further be correlated with the responses of vascular therapy (14), tissue hypoxia and hemodynamics (15), and active efficacy

of chemotherapeutic drugs (16). Furthermore, local thermoregulation may be associated with large value of nonnutritional component of blood flow (17), enabling specific recognition of cancerous traits.

Quantification of vascular structures and functional changes in microcirculation can be achieved through a variety of invasive and noninvasive vascular imaging systems. Invasive methods include microscopic analysis, such as immunohistochemistry, fluorescent imaging, and scanning electron microscopy of the biopsied tissue sample, which is typically a one-time procedure and may lead to changes in the host tissue physiology. High-resolution imaging of microvessel geometry and quantification of vascular density (VD) as well as branching order is possible using invasive methods, which is essential for elucidating vascular abnormalities (18). However, structural analysis with invasive methods is confined only to the small dissected section. The minimally invasive intravascular optical imaging methods, such as angioscopy and high-frequency optical coherence tomography (OCT), are also vital tools for endovascular imaging of

Significance

Existing procedures of screening subsurface cancers are either prohibitively resource-intensive and expensive or are unable to provide direct quantitative estimates of the relevant physiological parameters for accurate classification accommodating interpatient variabilities and overlapping clinical manifestations. Here, we introduce a handheld and inexpensive blood perfusion imager that provides a noninvasive in situ screening approach for distinguishing precancer, cancer, and normal scenarios by precise quantitative estimation of the localized blood circulation in the tissue over an unrestricted region of interest without any unwarranted noise in the data, augmented by machine learning–based classification. Clinical trials in minimally resourced settings have established the efficacy of the method in differentiating cancerous and precancerous stages of suspected oral abnormalities, as verified by gold-standard biopsy reports.

ENGINEERING

atherosclerosis structures, arterial embolism, and effects of stent-wall interaction (19, 20) involving cerebrovascular and coronary arterial diseases but are not sufficient for assessing functional changes such as blood flow or structural changes such as vessel density (18). Further, even minimally invasive methods are not ideal for critically ill and outdoor patients due to the associated complexity of device-related effects like bruising, soreness, and platelet aggregation. In addition, both invasive and minimally invasive methods are inept to offer a direct measure of functional changes in blood microcirculation.

While biopsy and subsequent histopathological examination remain to be the gold standard for cancer diagnostics, various noninvasive methods are progressively being explored for providing alternative means of screening and detection outside advanced laboratory settings for catering to the needs of the underserved. Further, unlike invasive methods, noninvasive assessments using positron emission tomography (PET) and MRI enable dynamic quantification of functional vascular parameters such as blood perfusion, blood volume and vessel permeability using suitable contrast agents (5). Noninvasive methods also maintain the physiology of host tissues. PET is considered a clinical standard for measuring metabolic parameters, blood perfusion, and blood volume, which are related to the clearance rate of radiotracers, but the quantification is often limited due to low spatial resolution, accuracy of the input function, and the model assumptions. Dynamic contrast-enhanced MRI provides an indirect measurement of vessel permeability and perfusion by linking with the strength of contrast uptake and washout parameters. However, these methods often depend on the flow and diffusivity of the contrast agent. Also, the measurement is semiquantitative in nature, resulting in ambiguities in interpretation, considering the fact that various perfusion parameters used for the analysis remain to be standardized (5). Further, PET and MRI systems are resource-intensive and not routinely available in community healthcare facilities.

OCT has of late emerged as a fast imaging method having spatial resolution between macroscopic and microscopic optical imaging systems, capable of providing cross-sectional or volumetric images of vascular structures at superficial locations up to penetration depth of 1 to 2 mm (21). In addition to characterizing structural changes, OCT augmented with special features such as spectral analysis (22) and Doppler shift algorithms (21) could also provide functional images depicting hemoglobin concentration and blood flow information, respectively. However, OCT probes and setups are sensitive optical imaging systems with limited field of view and often suffer from attenuation loss, revealing speckles and bright artifacts due to multiple scattering of light (23, 24). Further, OCT systems are commonly bulky and expensive and are not commensurate with the restrictive infrastructure inevitable in resource-limited settings.

Measurement of peripheral microvascular function is generically vital for interpreting various aspects of tissue physiology like hemodynamics, oxidative stress, muscle metabolism, claudication, ischemic ulceration, muscle mitochondrial injury, or gangrene due to reduced blood microcirculation and failure to meet the demand of tissue metabolism (25). Currently, other noninvasive optical devices like laser Doppler flowmeter (LDF) (26–28) and laser speckle (29) are used to assess peripheral vascular diseases and related conditions such as rheumatic diseases, sclerosis, dermal replacement, and oxygen therapy for wounds, but these methodologies suffer from their intrinsic limitations in terms of arriving at an unambiguous and explicit quantitative index of the microcirculation characteristics (17, 30). Patient-specific variations may also lead to anomalous predictions, considering significant noise in the signal resulting from randomly scattered light (30). Further, despite its widespread use, the voluminous nature of the instrumentation and a gross inability to provide quantitative information of the blood perfusion in terms of absolute units limit the efficacy of LDF in decisive clinical applications (17).

Simple thermography images measuring the increase or decrease in tissue temperature may turn out to be viable alternatives toward pinpointing the mosaic of hypo- and hyperthermic locations associated with abnormal blood microcirculation in skin (31, 32), breast (33), and oral cancers (34). Premised on the postulate that cancer cells divide more aggressively than healthy cells by draining in nutrients and creating an alteration in the metabolic balance, local differentials in tissue temperature, obtained around surface or subsurface lesions in the human body via contactless thermographic imaging procedures, may lead to the identification of cancerous traits in a rather elegant manner. However, these are likely to provide only an indirect and nonspecific interpretation of malignancy-associated alteration in the blood perfusion or otherwise. Physically, the measured tissue temperature varies with the surrounding ambient temperature and humidity and due to tissue blood perfusion and metabolism. Hence, the tissue temperature measurement by thermography alone is often not reliable for quantification of the diseased state of the tissue and cannot be considered as a fundamental depiction of the underlying pathophysiology because of its sensitive dependence on several other relevant parameters impacting the selectivity of prediction. Reported thermographic studies revealed elevation in the surface temperature of an oral lesion and its periphery, which is mainly due to hypervascularity (35, 36). However, due to lack of explicit mapping with malignancy-associated changes in the blood microcirculation, such events in the thermogram did not emerge to provide an essential classification between plausible alternative states of health and disease in an affirmative manner. This deficit may be attributed to an unaddressed specific correlation between the temperature and vascular growth features. As a consequence, surface temperature data may need to be augmented with some more specific attributes and parameters for confirmatory differential diagnostics between visually deceptive and overlapping presentations of the disease, in particular an accurate classification of precancer, cancer, and normal scenarios. Blood perfusion data, derived from the tissue temperature and other relevant considerations, may therefore offer a viable proposition to mitigate this challenge, by explicitly and specifically linking with the physiological features of the identified lesion or any other form of suspected abnormality.

Commercially available blood perfusion imagers (BPIs) are typically expensive. Further, these commonly offer relative readout of the perfusion data in arbitrary units (or in voltage units in some cases) over a restricted region of interest only. To circumvent these constraints, it may be imperative to develop a broad-field imaging-based screening tool fundamentally premised on the blood perfusion data in absolute units of physiological reference (i.e., milliliters per minute per 100 g of tissue). This value-added proposition, in conjunction with powerful optical (37) or thermometric sensors (38), may provide a decisive quantitative index of localized microcirculation consistent with clinically proven "gold standards" (5, 17, 30). This, along with the emergence of a user-friendly and inexpensive portable detection unit for thermal image acquisition and data integration, may enable the technology to perform a simple, inexpensive, quantitative, and noninvasive in situ screening and diagnostic procedure for evaluating the disease with an envisaged high level of accuracy in resource-limited settings, avoiding erroneous differential diagnostics between potentially ambiguous scenarios.

While blood perfusion imaging devices are not uncommon in sophisticated clinical settings with adequate infrastructure and human resource support, their affordable parallels for use at underserved locations with uncompromised predictive accuracy remain elusive. Availability of the latter may emerge as an

2 of 12 | PNAS
https://doi.org/10.1073/pnas.2026201119

Bhowmik et al.
Portable, handheld, and affordable blood perfusion imager for screening of subsurface cancer in resource-limited settings

exclusive value-added decision-making tool for public health management, considering that it may not be trivial to come up with an accurate classification on the malignant state or otherwise of the observed abnormalities during clinical examination, purely by appealing to "trained eyes and hands." Such a "clinical dilemma," as per the present state of the art, can be resolved to confirmation only by appealing to invasive and resource-intensive biopsy-based procedures that are otherwise extremely rare facilities to be made available in primary health settings. However, whereas the development and advancement of a simple BPI may add a decisive value proposition to this cause, the same may alone not be adequate considering the subjectivity in manual interpretation of the obtained images. Therefore, it is further imperative to develop a machine learning (ML)-based classification algorithm that applies on the physics-based blood perfusion data derived from the thermal images and in turn accurately classifies different types of potential tissue abnormalities and lesions in a clinically decisive manner.

Here, we introduce a portable and user-friendly BPI that combines a miniature far-infrared (FIR) camera and a humidity sensor, which are electronically controlled and interfaced with a combined physics-based and data-driven software engine, with a vision of classifying cancerous and different noncancerous traits in an identified subsurface tissue in vivo which can be deployed in resource-limited settings. The thermal analytic procedure of the device combines coordinated simultaneous readout of pixelated tissue temperature, as well as temperature and humidity of its immediate surroundings, to arrive at a precise quantification of blood perfusion in terms of absolute physiological units from the thermal image data. Toward this, the measured tissue temperature distribution acts as an input field data to construct the blood perfusion map using a blood perfusion correlation (BPC), which is developed based on a physics-based equation (bioheat transfer model). The data of temperature and humidity incipient to the tissue here act as inputs to develop this correlation via a simple inversion approach. Realistic depictions of blood perfusion measurement in absolute units, as obtained from the present device, are confirmed by comparing with reported practical ranges of blood perfusion in oral tissues (*SI Appendix,* section S8).

Subsurface cancer such as oral cancer, at its early stage, is known to manifest an increase in blood perfusion, whereas a full-grown cancer reveals decrease in blood perfusion similar to precancer or normal cases. Accordingly, clinical classification based on either visual inspection or even by naïve blood perfusion imaging in many situations is likely to result in misclassification due similar deceptive features among certain stages of cancer and precancer, and even other completely temporary artifacts. One major aspect of this confusion stems from interpatient variability that leads to potential misclassification. This present technology, accordingly, is further augmented with an ML algorithm designed for automatic classification of fine-grained variability in the captured images that are not visually distinguishable on the surface. Toward this, an ML-based algorithm is developed with a group of classified blood perfusion maps as training datasets, to avoid misclassification associated with interpatient variability. It needs to be mentioned here that ML is employed with the sole purpose of accurately classifying the study groups as per a training-based classification algorithm but is in no way used to determine the blood perfusion values. Finally, "untrained" blood perfusion data are classified using the developed ML, where the physics-based blood perfusion map acts as input and the disease classification as the output. Premised on the principle of local change in blood microcirculation's being associated with the metabolic need of the lesions at different growth phases (12, 13) and the alteration of thermal field as a consequence of local thermoregulation (33), this ML-augmented approach executed in community healthcare-based settings is proven to report unambiguous differential classifications of cancerous and precancerous traits, as validated by double-blinded clinical trials with the gold-standard biopsy data as the benchmarking reference. Further, going beyond the specific scope of diagnosing superficial lesions, the present method opens up newer possibilities of arriving at a generic principle of contrast-free and accurate mapping of a variety of diseased traits by establishing correlation with complementary evidence-based principles (39–42).

Results

Design and Operation of the Blood Perfusion Measuring Device.
The design and operation of the blood perfusion measuring device are shown in Fig. 1*A*. The prototype assembly is shown in *SI Appendix,* section S1. The design consists of a probing unit for screening and a processing unit for obtaining blood perfusion data and disease recognition. The probing unit is composed of a three-dimensional-printed holder and sensor housing, such that the holder is used for guiding the sensor housing to the measurement site (Fig. 1*B*) and the sensor housing is used to maintain a stable environment for sensors to minimize the effect of breathing. The sensor housing consists of an on-chip FLIR Lepton 3.5 long-wave infrared (IR) camera (FLIR Systems Inc.) for measuring tissue temperature and a fully calibrated digital humidity sensor HTU21D (Measurement Specialties, Inc.) for measuring ambient temperature and relative humidity. The IR camera sensor array captures the spectral radiance in the wavelength range of 8 to 14 μm and uses additional signal-processing electronics to convert the radiometric values into temperature value with thermal sensitivity <50 mK and for imaging at a rate of 8.7 Hz. The camera is calibrated with a linear temperature calibration equation (*SI Appendix,* section S2) determined by fitting the temperature data of a reference black body measured using the camera and that of a thermocouple.

The acquisition platform uses an external processor, which passes the raw data, i.e., immediate surrounding temperature and relative humidity, from the humidity sensor to the processing unit. These data are accessed using a computer by establishing a remote connection with the external processor. The device operation is shown in Fig. 1*C*, wherein the motion artifacts in raw thermal image sequences are stabilized using image registration steps. Each pixel of thermal image sequences is calibrated by a temperature calibration equation. Subsequently, the pixel value of the thermal image for each time instant is automatically scanned in a raster fashion and is processed through a routine composed of BPC, wherein the blood perfusion images are quickly extracted from raw data with the aid of an iterative computational algorithm. The BPC correlation (see *Materials and Methods*) is effectively obtained by developing a physics-based semianalytical solution that is premised on the bioheat equation and the associate thermal boundary conditions (see *SI Appendix,* sections S4–S6 for details). Data from the thermal imager to measure the tissue temperature field and the humidity sensor to measure the temperature and humidity of its immediate surrounding within the oral cavity are inputs to the BPC correlation deduced after simple analytical inversion of the bioheat equation. Accordingly, the tissue temperature distribution measured by the thermal imager is used to construct the underlying blood perfusion maps, with the ambient temperature and humidity within the oral cavity measured by the temperature and humidity sensor, respectively, acting as the boundary conditions. This modeling approach accounts for an obvious variation in the tissue temperature specifically due to in vivo blood perfusion and metabolism. The BPC correlation normalizes the effect of the immediate surroundings to
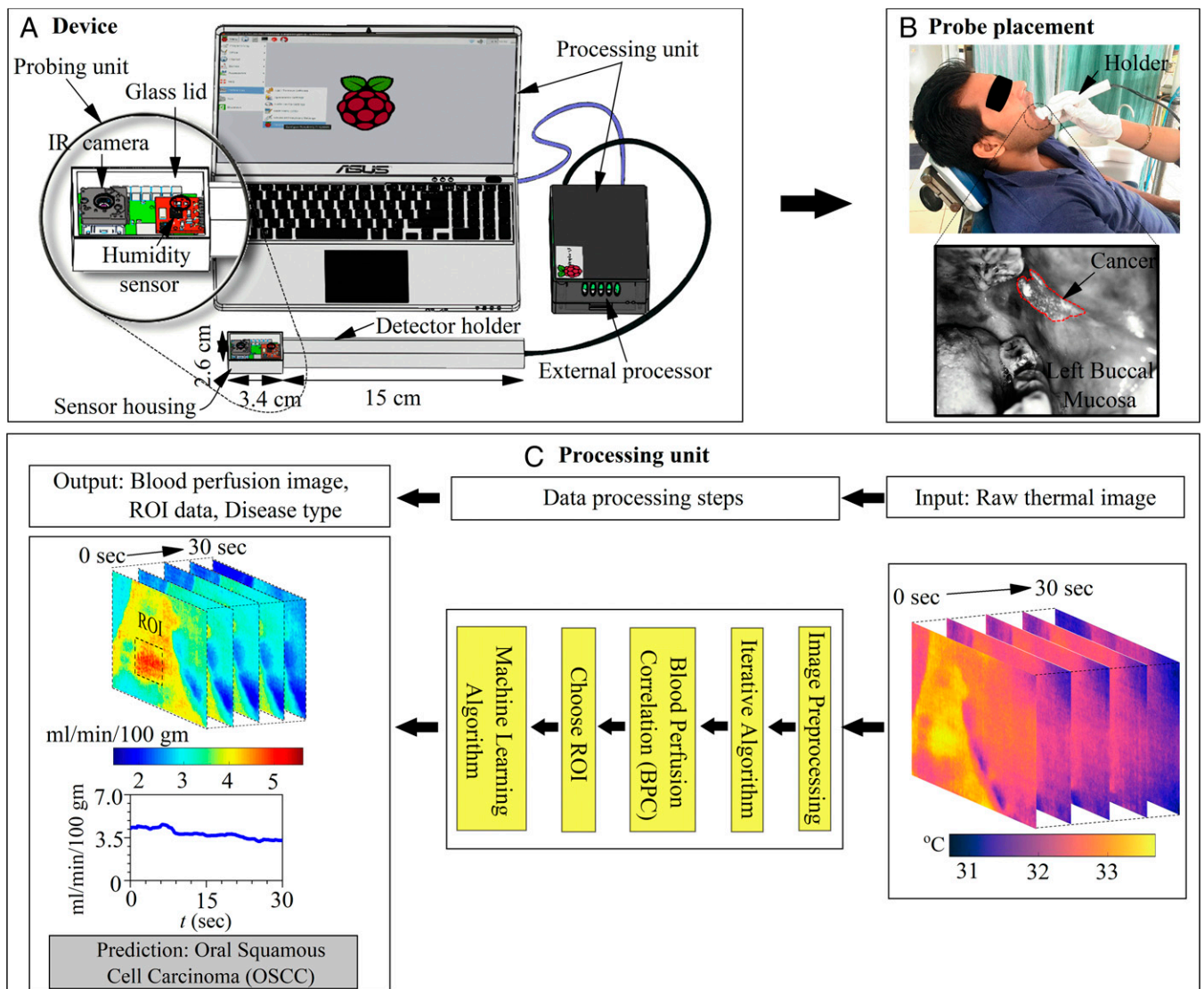
Bhowmik et al.
Portable, handheld, and affordable blood perfusion imager for screening of subsurface cancer in resource-limited settings

PNAS | 3 of 12
https://doi.org/10.1073/pnas.2026201119

Fig. 1. BPI overview. (*A*) Design specifications of blood perfusion imaging device and a magnified layout of the sensor housing with an FIR camera and a humidity sensor controlled by a computer and external processor. (*B*) An illustration of oral cancer screening with the device. Here, a patient is lying in a decubitus-supine comfortable position on a dental chair and the probe head is placed within the oral cavity for screening of LBM. The right-hand posture, i.e., a comfortable grip on the device and support on the patient's face using the operator's fingers is a useful practice to avoid movement of the device during screening. (*C*) Operational steps to extract the absolute value of blood perfusion and automatic disease classification using an integrated ML algorithm.

extract the absolute value of the blood perfusion from the measured tissue temperature field that has obvious dependence on its surrounding conditions.

Finally, the blood perfusion image data corresponding to the region of interest (ROI) are passed through a robust ML algorithm to recognize and screen the target disease conditions. This ML algorithm has been trained by classified blood perfusion images of oral cavity cancer and precancer as a training database, authenticated by combined clinical examination and biopsy reports as performed and supervised by specialist experts, to avoid misclassification associated with interpatient variability among the study groups. Finally, "untrained" blood perfusion data are classified using the developed ML for assessing the predictive efficacy of the method developed, where the physics-based blood perfusion map acts as input and the data-driven disease classification acts as the output. The details of the ML algorithm are discussed in *Materials and Methods*. For the image registration step, formulation of modified bioheat

equation, analytical solution, and iterative computational algorithm constituting the physics-based equation please refer to *SI Appendix*, sections S3–S7.

Spatiotemporal Variation in Blood Perfusion of Oral Cancer and Precancer. Here, we demonstrate a clinical application of our method for differentiating oral squamous cell cancer (OSCC) and oral submucous fibrosis (OSF) from normal tissue, based on measured changes in blood perfusion undertaken in a non-invasive manner. OSF is a commonly found precancer in the South-Asian population, which is often identified clinically based on visual/palpable inspection of submucous fibrosis and difficulty in opening the mouth. Also, OSF with dysplasia shows a high rate of malignant transformation (43). Currently, noninvasive diagnostic tests that offer a quantitative evaluation of the underlying condition are limited. We initially measured the baseline value of blood perfusion for 10 different oral sites of normal participants (*SI Appendix*, section S8) and quantified

the deviation from the baseline range due to the presence of OSCC and OSF in the similar oral sites.

It is important to mention here that one major study objective of the clinical trial undertaken for oral cancer screening is to establish the proposition of precise classification among three different patient groups (normal, OSCC, and OSF) based on the measured blood perfusion data. Accordingly, a set of confirmed cases of participants in the clinical study is first allocated in each group with the sole objective of creating a dataset for training the ML algorithm developed for disease classification, according to the inclusion criteria as detailed in *Materials and Methods*. Here, analysis and interpretation by a qualified clinical expert and supportive confirmatory diagnostic information are utilized for labeling the input blood perfusion images during the training of the ML algorithm. Once the training of the ML algorithm is complete, the validation of the method is carried out using a randomized unlabeled image dataset inclusive of newly captured images that were not used for training the ML algorithm to avoid any bias in disease recognition and classification. The obtained sensitivity and specificity values, as an outcome of this clinical trial, thus reflect the resulting accuracy of disease classification from the double-blinded dataset. The efficacy of classification has independently been verified by the gold-standard procedure executed by the expert clinicians on the sample cohort.

Fig. 2 *A–C* depicts the clinical, thermal and blood perfusion maps of a healthy individual and individuals with OSCC and OSF, respectively. The spatiotemporal maps cover a wide area inside the patient's mouth and reveal demarcations in blood perfusion among the individual patients, thus enabling a qualitative comparison of malignant and premalignant changes from the images. Here, the individual with OSCC shows higher blood perfusion in the symptomatic site in contrast to normal and OSF (Fig. 2*D*). The maximum and minimum values of spatial line graphs in Fig. 2*E* indicate blood perfusion of the highly vascularized region (i.e., center/perilesion area) and relatively less vascularized surrounding healthy region, respectively. In Fig. 2*F*, BPC correlation fidelity is established, displaying good fit between predicted temperature by a finite element method (FEM) model and measured temperature of the lesion.

Comparison with the Gold-Standard Method. Next, we performed a qualitative comparison between blood perfusion images, clinical observation, and histopathological findings to establish a connection with a disease condition. Fig. 3 depicts clinical, thermal, blood perfusion, and histological images of normal, OSCC, and OSF patients. Participant 1 (Fig. 3*A*) is a healthy male with no signs and symptoms of systemic disease or oral lesion. Participant 2 (Fig. 3*B*) is a male with OSCC extending from the left oral commissure region to the buccal mucosa. The lesion is ulcerated and has an irregular floor and margins, with exophytic white necrotic uneven crust formation. Participant 3 (Fig. 3*C*) is a male with OSF of the buccal mucosa. Both the right buccal mucosa (RBM) and left buccal mucosa (LBM) have a blanched, opaque, blotchy marble-like appearance along with a firm, coarse, and palpable vertical fibrotic band. Participant 3 also reported a burning sensation and progressive reduction of mouth opening, and the measured interincisal distance was ∼3.0 cm. Blood perfusion values of Participants 1 through 3 (Fig. 3 *G–I*) vary approximately in the range of 2 to 8 mL·min^{-1}·100 g^{-1} in healthy tissue, exhibiting a mosaic of low and high value in the region involving OSCC and an overall reduction in the value in OSF case. In the case of OSCC (Fig. 3*H*), white, firm, keratotic regions indicate less perfusion as compared to the adjacent ulcerated and necrotic region. In the case of OSF (Fig. 3*I*), the overall reduction of the tissue temperature and blood perfusion are likely to be an indication of obliterated or narrowed blood vessels due to increased fibrosis
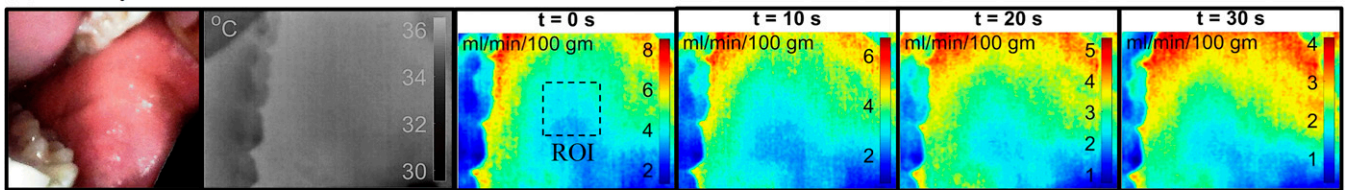
of the tissue (43). In all these cases, confirmation of disease states was made by an experienced oncopathologist with the aid of clinical and gold-standard hematoxylin/eosin-stained light microscopic features as depicted in Fig. 3 *J–L*. For disease confirmation, histological features such as shape of rete ridges, thickness of epithelium, existence of inflammatory cells, and degree of fibrosis/hyalinization have been considered. Normal tissue (Fig. 3*J*) shows V-shaped rete ridges and negligible inflammatory cells. The OSCC cases (Fig. 3*K*) reveal loss of epithelium, manifestation of malignant islands, and increase in inflammatory cells. The OSF cases (Fig. 3*L*) exhibit epithelial atrophy and significant subepithelial hyalinization and display a flat interface across epithelium-connective tissue and an increase in inflammatory cells.

In most cases of OSCC, we have observed intra- and interpatient heterogeneity in lesion blood flow rates with 1) significantly high blood perfusion at its center/perilesion area as compared to surrounding normal tissue in its developing stage and 2) poor/similar blood perfusion over lesion compared to its surrounding for grown tumor or tumor originated from earlier history of OSF (*SI Appendix*, section S9).
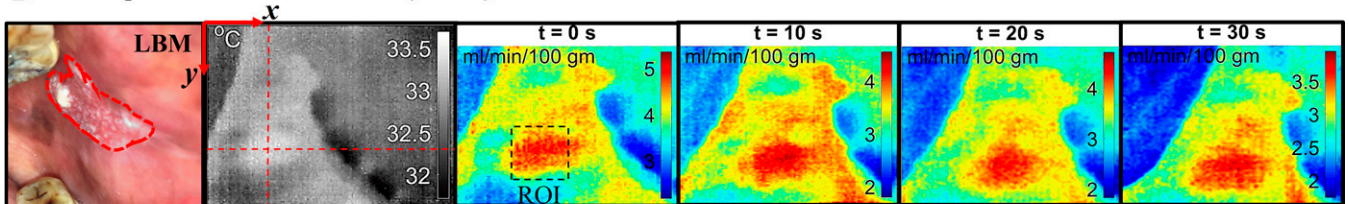
Quantification of Blood Vessel Structures Using OCT as a Complementary Multimodal Image Analytic Approach. Since, unlike the present device, the existing commercial devices are not capable of providing the blood perfusion data in absolute units, direct validation of the obtained blood perfusion values in terms of measured changes with or without lesion is not possible. Hence, we have presented an indirect parallel assessment of the final diagnostic recommendation (which is the focus of interest so far as the utilitarian importance of the work is concerned) via correlating with the complimentary evidence corroborating measured changes in the lesion perfusion value with VD as measured by OCT-based imaging, in addition to validating with the gold-standard biopsy results. In this regard, it needs to be emphasized that the operational paradigm and principle of the present method and OCT are mutually exclusive, although the final predictive purpose in this context remains the same. In particular, whereas the present device provides the functional information (i.e., increase or decrease in blood perfusion), OCT provides the relevant structural information (i.e., changes in number of blood vessels at superficial locations) unless augmented by further complexities hallmarked by spectral analysis and Doppler shift investigation. While their scopes of specific nature of information obtainable are distinctive, these may clearly act as complementary approaches to arrive at decisive information on a specific diseased state as per the scope of this work. Such a paradigm of multimodal analytics for diagnostic and clinical decision-making is becoming increasingly more prominent for disease detection and management in the modern digital era.

By employing the BPI and OCT we have thus performed a parallel comparison in a multimodal format between the aspects of the disease-associated functional changes (blood perfusion) and structural changes (vessel density and area) to arrive at a well-correlated framework. The interpatient deviation in pixel-averaged blood perfusion (ω_b) value of OSCC and OSF groups from the normal group involving the RBM and LBM is shown in Fig. 4 *A* and *B*. The two subframes of time series blood perfusion in Fig. 4*A* indicate higher values prevailing among OSCC participants compared to normal groups, whereas the OSF groups indicate an opposite trend. The observed decay in time series in blood perfusion data are mainly due to the fact that the real-time thermal imaging on the patient was carried out in a dynamic condition starting from the closed position to the open position of mouth, albeit in a slow transition mode. This led to a small but dynamic change in the tissue temperature and the boundary conditions
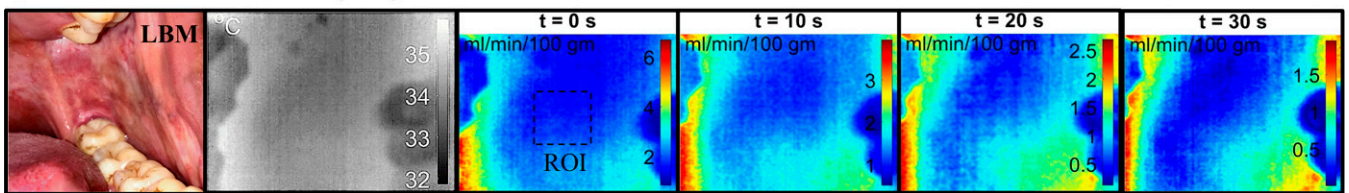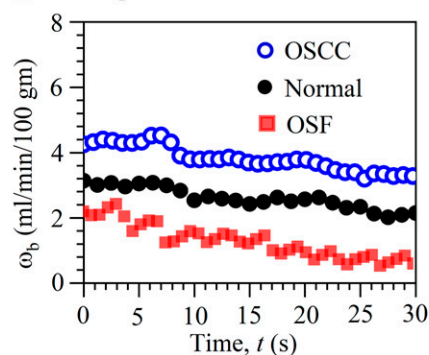
Bhowmik et al.
Portable, handheld, and affordable blood perfusion imager for screening of subsurface cancer in resource-limited settings

PNAS | 5 of 12
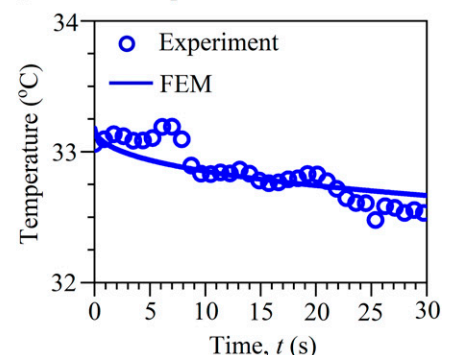https://doi.org/10.1073/pnas.2026201119
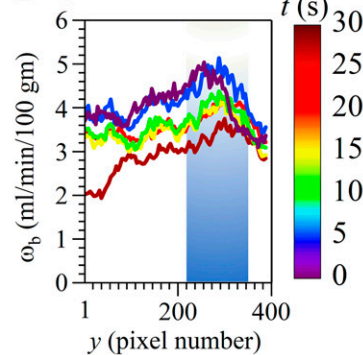
Fig. 2. Local variation in blood perfusion and tissue temperature of normal, OSCC, and OSF participants. Clinical, thermal, and spatiotemporal maps of blood perfusion of (*A*) healthy individual (34-y-old male) and individuals with (*B*) OSCC (82-y-old male) and (*C*) OSF (45-y-old male) involvements in the LBM revealing alteration in malignant and premalignant changes in perfusion. (*D*) Measured well-defined deviation in time series blood perfusion (ω_b) among individual patients with OSCC and OSF involving LBM (represented by pixel-averaged value of the ROI shown in *A*–*C*). (*E*) Spatiotemporal variation of blood perfusion in the y direction along the red dashed line in thermal image *B*, indicating peak value at the lesion center/perilesion area. (*F*) Measured temperature at the surface of the oral mucosa above the OSCC lesion along with predicted temperature by FEM using the blood perfusion value in *D*.

in its immediate surroundings, influencing the in vivo blood perfusion. However, this dynamic variation remained effectively consistent for all the patient trials. Accordingly, a 3-min stabilization/equilibration pause was adopted for the diagnostic procedure, as discussed in *Materials and Methods* (*Methods Applied to Imaging Intraoral Sites*). We also performed a unit root test on the mean of time-series data using the "Augmented Dickey–Fuller" method to identify whether the time-series data exhibited a stationary trend or not and obtained the significance level of stationary trends ($P < 0.007$), indicating statistical significance. However, the SD/error of time series data failed to reject the unit root test revealing a nonstationary trend.

The paired comparison of pixel averaged blood perfusion of different study groups by box-and-whisker plot (Fig. 4*B*) indicates significantly higher blood perfusion ($P < 0.001$) for OSCC as compared to the normal group in LBM, and the OSF group displays significantly lower blood perfusion values ($P < 0.001$) as compared to the normal group in RBM and LBM, respectively. Fig. 4*B* also reveals overlapping feature in blood

perfusion value due to interpatient variability in the lesion blood flow. We have also performed manual classification of each pair by defining a blood perfusion threshold value (τ) within the range of blood perfusion in the box-and-whisker plot (*SI Appendix*, Fig. S13). However, the manual classification is observed to underperform in distinguishing the class (or patient conditions) within the pairs due to overlapping in blood perfusion data. We have also performed a parallel comparison using thermal image data and blood perfusion data. Direct use of thermal images leads to less sensitivity and specificity in disease classification while using tissue surface temperature as the sole basis of interpretation (*SI Appendix*, Fig. S11) as compared to blood perfusion data. To overcome the poor performance of manual classification, we have further incorporated an automated computer-aided classification of diseases using an ML algorithm (see Fig. 5). It can be noted here that the plausible contrasting predictive features depicted in Fig. 4 as opposed to the ones subsequently presented in Fig. 5 stem from the fact that the blood perfusion remains to be only one feature out of
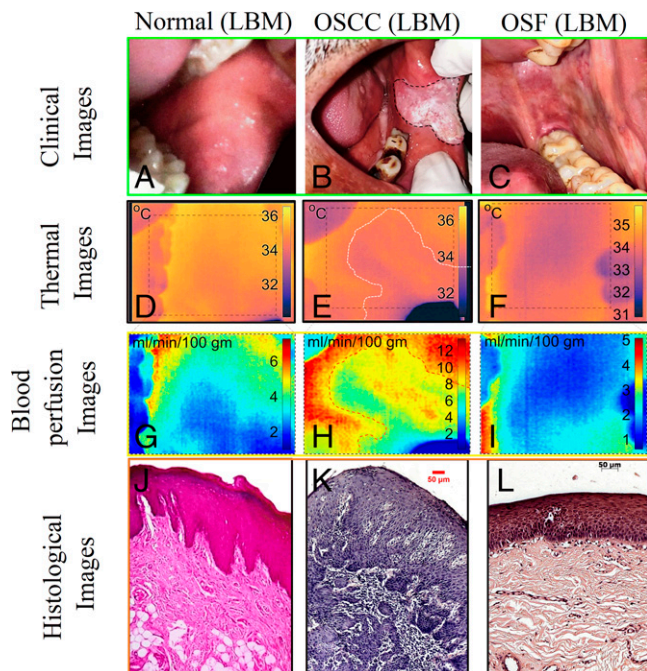
Bhowmik et al.
Portable, handheld, and affordable blood perfusion imager for screening of
subsurface cancer in resource-limited settings

Fig. 3. Montage representing clinical (*A–C*), thermal (*D–F*), blood perfusion (*G–I*), and histological images (*J–L*) of healthy, well-differentiated OSCC, and OSF tissues. For interpretation, the rows represent the image type and columns represents the cases, i.e., healthy, OSCC, and OSF, respectively. The representative images are from a common site, i.e., LBM, which corresponds to different participants (participant 1: healthy male, 34-y-old, participant 2: male, 57-y-old with OSCC, and participant 3: male, 45-y-old with OSF). Here, the histological images were presented with original magnification of 10×. The healthy area of the oral mucosa is well-perfused and indicates high temperature. The area of cancerous lesion indicates mosaic of high and low temperature and/or blood perfusion (*E* and *H*). The fibrosis case indicates significant reduction in overall blood perfusion and tissue temperature (*F* and *I*).

several considered for the ML-based interpretation. The fact that the latter has been trained to use about 20 image and data features for the desired classification rationalizes possible contrasting interpretations from ML- and non-ML-enabled decision-making procedures for any identified patient hallmarked by visually ambiguous data presentation.

Fig. 4*C* is a demonstration of image analysis steps adopted to extract the in situ vascular parameters from raw OCT images of tissue sections. Initially, the raw OCT image of the buccal mucosa is preprocessed using low-pass spatial filtering and an intensity transformation method to remove the speckle/noise and enhance the image contrast, respectively. Then, an image segmentation operation is executed to segment the vascular structure from immediate background. After segmentation, the vessel region properties are extracted from the segmented image to evaluate the VD and total vascular area (TVA) (*Materials and Methods*). The processed OCT images of a patient during image analysis are also shown in Fig. 4*C*, such that the raw image (top) is followed by segmented images with and without traced vessel boundaries, and finally the original image is displayed with the fused boundary mask of traced vessels (bottom). A comparison between OCT images of OSCC and normal buccal mucosa reveals an overall increase in red-colored vascular structures (Fig. 4*D*). However, processed OCT images of OSF involving the buccal mucosa reveal fewer stretched vascular structures due to fibrosis. This trend is found to be consistent with the VD and TVA extracted from segmented OCT images (Fig. 4 *E* and *F*), revealing a significant difference in VD and TVA among the groups ($P < 0.05$) except for TVA occupied by normal and

OSCC cases. It clearly implicates 1) an increase in vascularity in the case of malignant lesion (44), and 2) obliterated or significant narrowing of the vessels in subepithelium of OSF cases due to fibrosis (43). In fact, we have identified not far off linear correlation between functional changes in the microcirculation (indicated by blood perfusion) and that of the structural variation in vessel density (Fig. 4*G*) narrating the reason behind reduced blood microcirculation for the OSF cases.

High-Throughput Screening of Diseases Using the ML Algorithm. To automate the disease recognition process as well as to overcome the misinterpretation inevitable with manual classification, we have integrated a robust multiclass classification model based on an ML algorithm (Fig. 5) which enables automatic and accurate classification of normal, OSCC, and OSF for all oral sites based on blood perfusion images taken by the device. Fig. 5*A* demonstrates the method employed for automatic classification of disease cases (*Materials and Methods*). We have compared the accuracy of three different classification models: multiclass support vector machine (*m*SVM), *k*-nearest neighbor (KNN), and ensemble of learners (ENS) in Fig. 5*B* for the entire image pool, training image pool, test image pool and new image pool separately. The confusion matrices for each image pools are separately shown in *SI Appendix*, Fig. S14. Except for the ENS model, all other classification models reveal higher misclassification of the newly grabbed blood perfusion image pool. Particularly, the ENS model (Fig. 5*C*) accurately predicts 100% of normal and OSCC cases and 96.6% of the OSF cases; 3.3% of OSF was misclassified as OSCC in the unlabeled data pool. The ENS model also indicates overall high sensitivity (true positive rate) >96.66% and specificity (true negative rate) 100% in distinguishing one class from other two classes as shown by the receiver operating characteristic (ROC) curve (Fig. 5*D*). Here, the sensitivity and specificity values refer to the overall validation accuracy of the best-performing algorithm to accurately identify disease classes from the unlabeled "double-blinded" dataset maintained and analyzed by clinical experts, with supportive evidence from combined clinical examination and gold-standard biopsy.

The algorithm has also achieved the desired accuracy in marginal cases that are not visually discernible (see *SI Appendix*, Fig. S15 for illustration). In fact, the inclusion criteria of our study covered a variety of marginal cases wherein the inflammation could not be visually classified by even highly experienced clinicians without ambiguity. For example, some marginal cases revealed negligible visually discernible difference between normal and OSF. In addition, the clinically demarcating feature of "interincisal distance" appeared to be virtually indistinguishable, and no conclusion could be arrived at on palpation of the suspected tissue site as well. This ambiguity on clinical examination created confusion to even highly trained and experienced doctors. Such ambiguities could be resolved by appealing to the diagnostic screening technology developed and advanced herein and were finally confirmed by gold-standard biopsy.

The demonstrated capability of differential diagnosis of OSF reasonably early, when the visual features remain indistinguishable from normal scenarios, is extremely critical for public health management at under-resourced locations, since further complexities in the disease progression may lead to irreversible damage as well as transformation to malignancy via epithelial-to-mesenchymal transformation. The potential lifestyle disruption, if allowed to progress indefinitely, may lead to an inability of the patient to open the mouth at a later stage. However, if the disease is detected early, cessation of the chewing/other adverse oral habit along with rounding-off sharp teeth and extracting third molars may be adequate means of disease management without further complications. As a more recently introduced therapeutic intervention, intralesion injection of
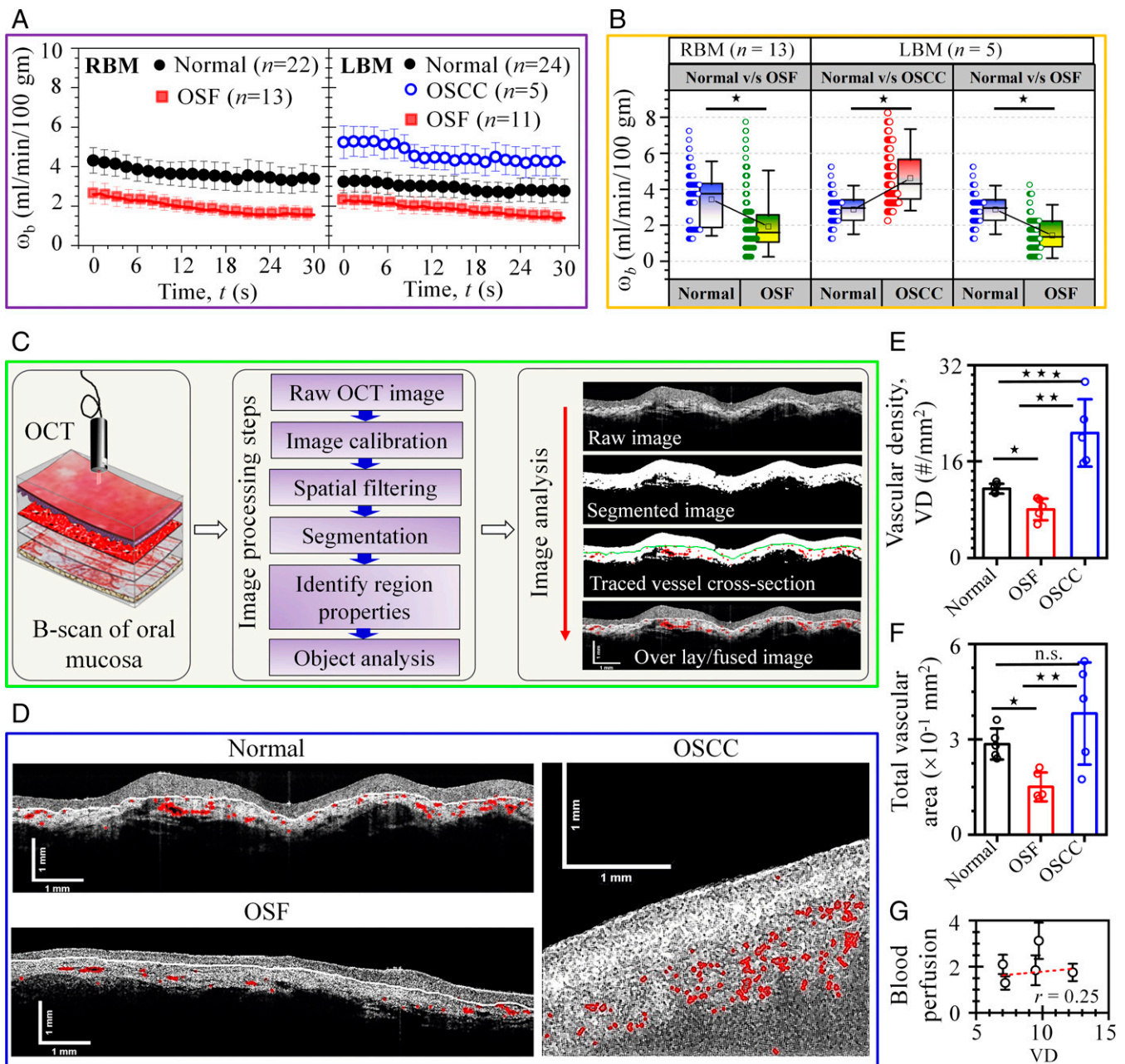
Bhowmik et al.
Portable, handheld, and affordable blood perfusion imager for screening of subsurface cancer in resource-limited settings

PNAS | 7 of 12
https://doi.org/10.1073/pnas.2026201119

ENGINEERING

Fig. 4. Disease-specific variability in blood perfusion and structural vascular parameters. (*A*) Time series data (mean ± SE) of blood perfusion (ω_b) comparing normal, OSCC, and OSF tissue of RBM and LBM, respectively. The two subframes of time-series data correspond to average of pixels in the ROI presenting higher value of perfusion for OSCC and normal cases as compared to OSF. (*B*) Box-and-whisker plot differentiating measured pixel-averaged blood perfusion between different diseases classes in RBM and LBM used for quantification of the diagnostic test. Data revealed statistically significant differences in the time-series data of blood perfusion (*$P < 0.001$). (*C*) Image processing steps adopted for extraction of vessel structural parameters (i.e., VD and vascular area) from OCT images of tissue section. (*D*) Qualitative comparison between fused OCT images of buccal mucosa of patients indicating an overall reduction and increase in red-colored vascular structures in OSF and OSCC case, respectively, as compared to the normal case. (*E*) Disease-specific alteration in VD (mean ± SD; *$P = 0.009$, **$P = 0.009$, ***$P = 0.009$; $n = 5$). (*F*) Changes in TVA (mean ± SD; *$P = 0.009$, **$P = 0.028$, n.s., not significant; $n = 5$). (*G*) Comparative evaluation of blood perfusion (mean ± SD) and VD of selected OSF patients indicating strength of linearity (Pearson's $r = 0.25$).

autologous bone marrow stem cells may also be effective in reversing such early stage of the disease via triggering angiogenesis leading to arresting the fibrosis and facilitating normalized mouth opening. However, since early detection of this remains unfeasible in healthcare practice in resource-limited settings in the current state of affairs, patients with OSF typically present with advanced disease progression, with inevitable irreversible damage. Results from the present study have clearly established the value in this regard by offering a community-level

measure toward arresting critical oral diseases at underserved locations.

We have further performed parallel comparison using the learners to predict disease classification accuracy while trained, tested, and validated for blood perfusion and thermal image data separately (*SI Appendix*, Figs. S12 and S14). It is evidenced that surface temperature data alone as an interpreter lead to more misclassification from an untrained pool of data as compared to blood perfusion data. These validations established
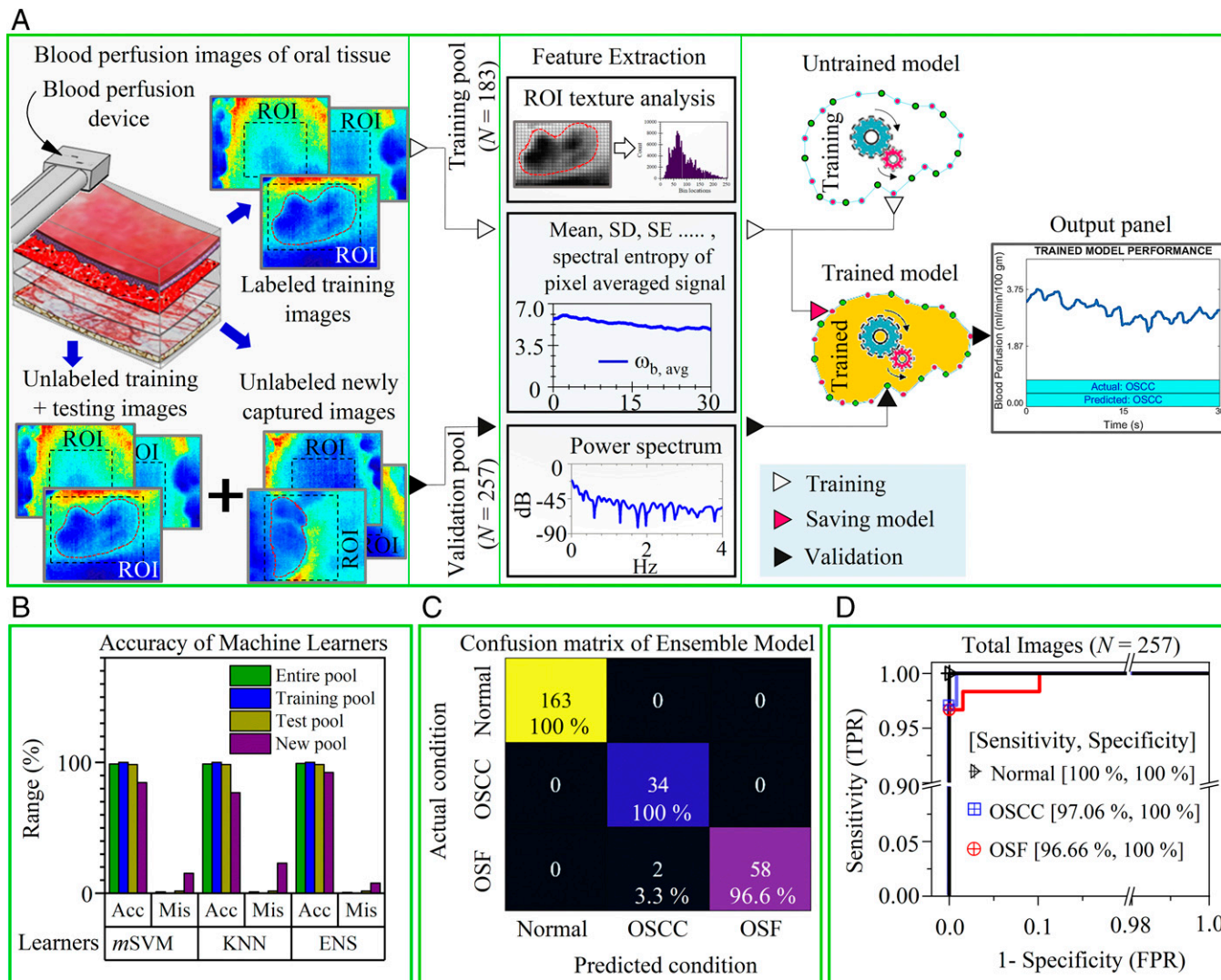
Fig. 5. ML-enabled OSCC and OSF recognition. (*A*) Overview of the training and validation process of the ML algorithm to recognize disease condition with high accuracy based on captured blood perfusion images by the device. Here, the training and validation dataset consist of images from all oral sites and the ROI was picked by the operator (or clinician) during acquisition to emphasis on the lesion area. These ROI are subjected to texture analysis and signal processing during feature extraction. The extracted features are passed to an unfitted machine learner with untrained parameters. Subsequently, the fitted model (or trained learner) could be saved and deployed as C or MATLAB scripts to the device processing unit for automatic classification. The model validation is ascertained by passing a pool of randomly distributed unlabeled images (i.e., training, testing, and newly acquired images) through a fitted model. The output console of the processing unit displays the actual and predicted conditions. (*B*) Comparison of disease detection results (i.e., accuracy [Acc] and misclassification [Mis]) by three different classifiers (*m*SVM, KNN, and ENS) of testing, the new and the entire image pool. (*C*) The heat map compares the actual condition (identified by clinical and histological features) and predicted condition identified by best learner (i.e., ensemble model) for the entire data pool (see *SI Appendix*, Fig. S14 for other pools). (*D*) ROC curve to represent the performance (i.e., true positive rate [TPR] and false positive rate [FPR]) of the ensemble model to accurately classify one class from other two classes. Areas under the curve for all curves were >0.98.

the accuracy of the blood perfusion imaging device augmented with the trained machine learner to distinguish disease classes accurately without any manual supervision. This successful demonstration further ensures the clinical potential of the present method and device for screening superficial cancer and precancer, featuring a quantitative method to noninvasively monitor malignant transformation and associated alteration in blood microcirculation without demanding specialized laboratory-based procedures.

Discussion

In the first possible clinical examination, any potential abnormality in the oral cavity may be manifested as lesions (malignant or premalignant) and also in other inflammatory forms.

Apart from malignant lesion (i.e., OSCC), there could be the four most common precancer conditions (OSF, oral leukoplakia, oral erythroplakia, and oral lichen planus) that could turn into malignant lesions at later times. On the other hand, trivially benign forms of inflammation could be manifested as white lining due to pressure of teeth on soft tissue, mouth sores, and painful ulcers. Further, some fewer common cases of sores and ulcers could arise due to poor oral hygiene (such as viral, bacterial, and fungal infections) and/or chemotherapy drug-induced cases. An experienced clinical expert attempts to distinguish potentially concerning oral lesions from common oral inflammation based on subjective factors like appearance, touch, high-risk oral sites (buccal mucosa, tongue, gum, palate, etc.), lesion duration, patient history, and response to preliminary medications. Often, in resource-limited settings, the mnemonic

Bhowmik et al.
Portable, handheld, and affordable blood perfusion imager for screening of subsurface cancer in resource-limited settings

PNAS | 9 of 12
https://doi.org/10.1073/pnas.2026201119

RULE (red and/or white lesion, ulcerated, lump, exceeding duration of 3 wk) is applied by the doctors/dentists as the sole plausible mode of screening of a potentially concerning lesion from other oral inflammation. However, with well-known vulnerable sources of misclassification, a compelling challenge turns out to be accurate characterization and assessment of the oral lesions where clinical ambiguities are deceptive.

Nonavailability of facilities with clinical acumen and supportive histopathological evaluation in resource-limited settings as a confirmatory decision-making tool make it immensely challenging to come up with an accurate classification of the observed abnormalities in tissues during clinical examination, when confronted with the above-mentioned dilemma. Considering these challenges, the BPI tool developed here has been perceived as a unique way of distinguishing oral cancer, precancer, and normal scenarios, with a clear impact on the distinctive clinical decision-making and therapeutic procedure that are to follow for malignant and nonmalignant yet vulnerable or threatening scenarios. Whereas the invasive biopsy procedure remains the only clinical gold standard to confirm such distinctions in established and resourced medical centers, the present device offers its value as a noninvasive and inexpensive screening tool to categorize various oral abnormalities in a resource-limited setting. The clinical trials presented here not only establish the efficacy of the method but also validate the fundamental scientific proposition that the alteration of thermal field of the potentially abnormal tissue location has a direct relation with the increase or decrease in blood perfusion depending on the localized growth features. Our analysis has further demonstrated congruence between the changes in lesion blood perfusion and that of in situ structural parameters such as vessel density and vessel area measured by optical biopsy method. This method, in a generic sense, also paves the way for contrast-free assessment of abnormal microvascular physiology, if integrated with more advanced medical thermometric devices such as microwave thermometry (39), ultrasound thermography (40), CT (41), and MRI (42) thermometry.

It also needs to be noted here that prior to this work methods suitable for fast and noninvasive diagnosis as well as differentiation of oral cancer and precancer have been implemented by saliva metabolic profiling as an altogether different approach (45). However, such an approach is expensive, sophisticated, and not ideal for underserved community and resource-limited clinical settings and is not a viable proposition for community-level screening. Circumventing those constraints, emergence of a simple, low-cost, hand-held device for rapid yet accurate screening of subsurface cancers and precancers holds utilitarian importance, considering the fact that cancer of the oral cavity is one of the major causes of morbidity and mortality among males and females in the underserved community, which reveals 80% chance of 5-y survival rate if diagnosed before metastasis; the survival rate drops to 65% or less in more advanced stages (46). The key reason for such reduced therapeutic outcome is the fact that most oral cancers are diagnosed at an advanced stage. From that perspective, the present technology offers an exclusive perspective of detecting the possible vulnerable cases early enough, possibly during the precancer stage itself, during a first examination by a clinician, to enable working out immediate therapeutic measures to ensure disease reversal.

The above-mentioned major bottleneck of oral cancer treatment and management, stemming from the failure of detecting the precancerous stage of the disease early enough, is likely to be circumvented to a great extent via integrating the ML-empowered automatic classification of fine-grained variability in the captured blood perfusion images that are not distinguishable visually. Whereas the invasive biopsy procedure remains the only clinical gold standard in established and resourced medical centers, the present method in this respect

has demonstrated its early success as a noninvasive and inexpensive screening tool to categorize various oral abnormalities in a resource-limited setting. Our clinical trials, thus, in addition to providing a quantitative insight on the method efficacy, established the value proposition that the inexpensive and portable device may be deployed in remote locations, as well as in low-resourced urban settings (for example, slums), for capturing the vulnerable cases early enough by raising serious concern among the clinician and patient and obviating any inattention. The screened vulnerable cases may eventually be subjected to confirmatory gold-standard biopsy procedure before administering the requisite therapy. As an inexpensive co-option to the standard and established clinical practices, this value-added tool is likely to strengthen the confidence of doctors in preliminary decision-making. Furthermore, the fundamental scientific premise of the present technique holds the potential of opening new vistas in rapid and affordable diagnostics of various other diseased conditions that can be uniquely mapped with precise quantitative alterations in localized microcirculation at surface and subsurface levels, including chronic pain, inflammation, vascular blood flow irregularities, and beyond.

Materials and Methods

BPC. Eq. **1** (see *SI Appendix*, section S4 for detailed derivation), as presented below, is a modified variant of the Pennes bioheat equation (47). It follows from the principle of local energy balance in the tissue as a combined consequence of thermal conduction, exchange of heat within the tissue due local thermoregulation via blood perfusion, and metabolic heat generation. It includes the thermal diffusivity α and the thermal capacity ρc as effective local properties, the latter being dependent on the blood perfusion itself, inducing an inherent nonlinearity in the governing equation:

$$\frac{\partial T}{\partial t} = \alpha_{eff}\left(\frac{\partial^2 T}{\partial z^2}\right) - \frac{\omega_b \rho_b c_b}{(\rho c)_{eff}}(T - T_b) + \frac{E_{O2}\phi_{O2}\omega_b}{(\rho c)_{eff}}. \quad [1]$$

Because of the nonlinearity mentioned as above, an analytical solution of Eq. **1** does not exist. However, considering an iterative framework on the basis of a guess value of the local blood perfusion, the effective properties may be ascertained to derive a closed-form expression satisfying Eq. **1**, which may be mathematically inverted (see *SI Appendix*, sections S5 and S6 for detailed derivation) to obtain a closed-form expression of the pixelated blood perfusion, $\omega_{b,(i,j)}$ corresponding to each grid point (indexed as i,j) of the measured thermogram stencil, referred to herein as the BPC correlation:

$$\omega_{b,(i,j)} = \left[\frac{(1-\Phi)h_{ov}}{\Phi\sqrt{k_{eff}\rho_b c_b}}\coth(\psi L_t)\right]^2$$
$$+ \left[\frac{h_{ov}}{C_3\sqrt{k_{eff}\rho_b c_b}}\sum_{n=1}^{\infty} A_n \cos\left(L_t\sqrt{\lambda_n^2 - \psi^2}\right)e^{-\lambda_n^2\alpha_{eff}t}\right]^2. \quad [2]$$

Various parameters appearing in Eq. 2, such as L_t, $\Phi\left[=\frac{\rho_b c_b(T_{i,j}-T_b)-E_{O2}\phi_{O2}}{\rho_b c_b(T_{amb}-T_b)-E_{O2}\phi_{O2}}\right]$, as well as the coefficients obtained as constants of integration are detailed in *SI Appendix*. The parameter Φ is function of measured tissue temperature ($T_{i,j}$) and the measured ambient temperature (T_{amb}) as obtained via thermal imaging, and $E_{O2}\phi_{O2}$ is referred to as an energy density parameter, wherein E_{O2} is the energy liberated by oxygen per unit volume of the oxygen consumed and ϕ_{O2} is the volume fraction of oxygen in the blood. T_b is the mean blood temperature which is a weighted average of surface and core body temperature $[=(1-\kappa)T_c + \kappa T_{i,j}]$, T_c being the body core temperature, κ is a weighting factor, h_{ov} is the overall heat transfer coefficient that encompasses thermal transport due to convection, radiation, and evaporation, ψ is related to thermal diffusion length scale of the perfused tissue ($=\sqrt{\omega_{b,g}\rho_b c_b/k_{eff}}$), α_{eff} is the effective thermal diffusivity $[=k_{eff}/(\rho c)_{eff}]$, k_{eff} is the effective thermal conductivity of the perfused tissue $[=(1-\phi_b)k_t + \phi_b k_b]$, $(\rho c)_{eff}$ is the effective thermal capacity of the perfused tissue $[=(1-\phi_b)\rho_t c_t + \phi_b \rho_b c_b]$, ϕ_b being the volume fraction of blood in the tissue ($\approx \omega_{b,g}\Delta t$), k_t is the thermal conductivity of the unperfused tissue, and ρ_b, c_b, and k_b are the density, specific heat, and thermal conductivity of blood, respectively. Here $\omega_{b,g}$ is the guess value of blood perfusion considered as a part of an iterative estimation procedure, to enable ascertaining numerical values of all the parameters appearing on the right-hand side of Eq. 2. The coefficients C_3, A_n, and λ_n represent a dummy variable, integration constant, and eigenvalues of the mathematical solution,

respectively. Expressions of these are included in *SI Appendix*, section S5. The input model parameters for measuring blood perfusion are tabulated in *SI Appendix*, Table S2. With these considerations, an iteratively updated value of blood perfusion, $\omega_{b,(i,j)}$, may be obtained explicitly at once, by appealing to the BPC correlation (Eq. **2**). The inner iteration at each temporal instant leads to rapid convergence to the true value of the blood perfusion at each grid point, at the specific time instant under concern, by adopting a fast iterative algorithm (*SI Appendix*, section S7). A time marching scheme following outer iteration is then employed with a time step of Δt (the time interval between the consecutive frames of the thermogram (= 0.125 s for a frame rate set to 8 Hz, for example), to obtain a spatiotemporal map of the blood perfusion data.

Supervised ML Algorithm for Automatic Disease Classification. As a part of the device processing unit, we integrated a robust ML model (Fig. 5*A*) which enabled automatic classification of normal, OSCC, and OSF cases with high accuracy, based on histogram/texture analysis and measured pixel-averaged temporal data $\omega_{b,avg}(t) = 1/(N \times M) \sum_{i=1}^{N} \omega_b(i,j,t)$ of the ROI, wherein the ROI was picked by the operator or clinicians. To train the model, an image pool involving all individuals was passed through statistical and signal processing functions in MATLAB to extract 20 features. These features are 1) maximum entropy and energy of the normalized histogram counts of the image ROI and 2) mean, median, absolute deviation, SD, SE, 25% and 75% quantile, interquantile, skewness, kurtosis, root mean square (RMS), root-sum-of-squares, peak-magnitude-to-RMS ratio, Shanon's entropy, spectral entropy, and maximum frequency and amplitude of power spectrum of the time series signal $\omega_{b,avg}(t)$. In relation to each training dataset, either of the three responses (i.e., normal or OSCC or OSF) was labeled based on confirmed clinical and biopsy report. Since the number of individuals of normal, OSCC, and OSF is distinct, the dataset was balanced by using the same data for OSCC and OSF two times to obtain a bias-free training dataset. We held out 25% of actual images as test dataset ($n = 61$) and 75% as training dataset ($n = 183$). Then, the labeled group of extracted features in the training dataset was used to train the classification models (mSVM, KNN, and ENS) separately to learn patterns for each response that are not recognizable by the human eye. To improve the performance of the classifier, we set high cost of misclassification for OSCC and OSF as compared to normal, implemented 10-fold cross-validation, and tuned the internal parameters of the classifier by invoking the Bayesian hyperparameter optimization. These steps were iterated a couple of times to obtain a robust classifier by discarding unwanted features, setting the high cost of misclassification, and employing different classification models. Finally, the trained model was saved that takes input as unlabeled images defined by the ROI and predicts the accurate response. In the validation step, apart from unlabeled training and test image pool, we used an additional 13 unlabeled images newly acquired by the BPI device that had never been seen by the saved model during training or testing. The ML algorithms for classification of disease condition is a modified version of example script provided by MATLAB central file exchange (48).

Study Ethics and Selection of Participants. The experimental procedure, detailed below, was designed to predict the site-specific deviation in the blood perfusion of OSCC and OSF, which is a precancerous condition, from healthy oral tissue and for comparative evaluation of the observation with gold-standard methods and in situ vascular parameters deduced from B-scan OCT images. These studies were carried out according to the ethical norms laid down by the Indian Council of Medical Research and World Health Organization, which was approved by the Institutional Review Boards of Guru Nanak Institute of Dental Science and Research (GNIDSR), Kolkata (Ref. No. GN/ADMN/19/023; Date: 1/21/2019), and Indian Institute of Technology Kharagpur (Ref. No. IIT/SRIC/DR/2019; Date: 2/5/2019). Following the ethical committee guidelines, each potential participant was first told about the imaging procedure and asked for their willingness to volunteer in this study. Upon willingness to participate and prior to imaging procedure, a signed written informed consent was collected from each participant along with history of systemic diseases in a separate form of survey/questionnaires. The study included 36 healthy volunteers, 14 individuals with OSF, and 11 individuals with OSCC, ages ranging from 20 to 85 y, irrespective of any gender bias, who fulfilled the inclusion criteria. All participants were divided into three study groups: healthy (Group-I), OSCC (Group-II), and OSF (Group-III) based on the inclusion criteria. Inclusion criteria included 1) healthy volunteers with or without oral habits, without any oral lesions and systemic diseases, 2) clinically diagnosed patients with OSF and OSCC who were scheduled for biopsy at a later date with their previous consent in the department of oral and maxillofacial surgery, GNIDSR, Kolkata, India for histopathological evaluation. Exclusion criteria included healthy volunteers not in normotensive status during imaging. OSF patients with a mouth opening of <2.5 cm were also excluded.

Methods Applied to Imaging Intraoral Sites. For imaging, participants were given full details of the experimental procedure and were instructed to rest in a decubitus-supine comfortable position on a dental chair, wherein the head position was immobilized. The participant was instructed to be relaxed, not to gesticulate, swallow, or speak, and to breathe normally during the procedure. The participants were instructed to open their mouth normally without any strain for 35 s during which the handheld detector was guided within the oral cavity by resting the hand on a support to minimize the motion artifacts in the image sequence of the investigating site. The detector housing and holder are made of biocompatible and biodegradable polymeric material polylactic acid, which was readily sterilized prior to its clinical use in each participant. For the healthy group, the imaging process was carried out in 10 oral sites with a stabilization pause for 3 min before each measurement. These sites are the anterior two-thirds of the dorsum of tongue (DT), left lateral border of the tongue (LLBT), right lateral boarder of the tongue (RLBT), ventral surface of the tongue (VST), RBM, LBM, lower labial mucosa (LLM), lower labial gingiva (LLG), left lower buccal gingiva (LLBG), and right lower buccal gingiva (RLBG). The entire experiment was performed during the early hours between 9:00 AM to 11:00 AM in an outpatient room. The ambient temperature and relative humidity inside the oral cavity differed from that of the room condition, and the measured ambient temperature and relative humidity by the humidity sensor was found to be in the range $33.507 \pm 1.503\,°C$ and $47.639 \pm 9.395\%$, respectively. The oral tissue moisture was measured using a digital moisture meter in the range of $85.05 \pm 3.412\%$. In selected participants, B-scan of OCT was acquired for comparison.

Methods Applied for Estimation of In Situ Vascular Parameters. We used a swept-source OCT system (OCM1300SS; Thorlabs Incorporated) operating at 1,325-nm central wavelength for imaging of buccal mucosa. Here, the vessel structural parameters (VD and TVA) were extracted from a standard two-dimensional OCT scan of buccal mucosa using an image processing step (Fig. 4*C*). The morphological features of blood vessels were extracted by segmenting the signal-free dark regions/blobs in the two-dimensional tissue images, which is supported by negligible light absorption by oxy- and deoxyhemoglobin of blood at 1,325 nm (49). The objective is to correlate the change in blood perfusion with that of the measured in situ vascular parameters obtained from OCT images. The methodology (Fig. 4*C*) for image analysis applied to raw OCT image is detailed here. Initially, the raw OCT image was converted to a grayscale image. Next, the image was calibrated based on measured maximum axial and depth dimensions, and area per pixel was computed by product of per pixel length in *x* and *y* directions. Subsequently, the speckle/noise in the grayscale image was smoothened by applying a low-pass Weiner filter with a correlation kernel of size 8×8 used for local neighborhood filtering operations of any pixel. The image contrast was enhanced by saturating 1% of the pixel data with low and high intensity of input image. After enhancement, we segmented the image using a multilevel Otsu's thresholding method for automatic identification of signal-free dark blobs or connected regions in the image, wherein multiple intensity threshold levels were determined from multimodal histogram distribution. The grayscale image is converted to binary image, such that all pixel values of the image above the specified intensity threshold value are assigned as "1" and other pixel values are assigned as "0." Further, an intermediate optional step was adopted to identify the coordinate of the epithelium-papillary layer junction for normal and OSF cases, which is often identified by the brightest junction in OCT images (Fig. 4*D*). However, this step may not apply to OSCC cases due to the absence of clear boundary, since cancer growth often corrupts the squamous epithelial layer. In this intermediate step, the algorithm performs a correction in the segmented binary image by closing all the dark region above the coordinate of the epithelium layer using a region fill operation. The correction step is essential to ensure no false identification of the vascular structures in the stratified squamous epithelial layer due to automatic segmentation operation, since epithelium is a vessel-free region. We further employed the connected component concept to identify multiple signal-free dark regions in the final segmented image and computed the region property such as vessel area, number of vessels (NV), total area of vessel (TVA), total area of tissue section, A_{ROI} (representing total area occupied by white pixel and included dark pixels), and VD, which is the number of vessel profiles per square millimeter of tissue section ($VD = NV/A_{ROI}$). Note that the A_{ROI} excludes the region that touches the outside edge of the segmented image using a clear border operation. Finally, we traced the region boundaries in the binary image to obtain a boundary mask and displayed the original image fused with boundary mask.

Histological Examination. Following the imaging procedure, biopsy was performed under local anesthesia from the representative sites of all the selected study subjects with prior consent and medical fitness, in the department of

Bhowmik et al.
Portable, handheld, and affordable blood perfusion imager for screening of subsurface cancer in resource-limited settings

PNAS | **11 of 12**
https://doi.org/10.1073/pnas.2026201119

ENGINEERING

oral and maxillofacial pathology of GNIDSR, Kolkata, India. All the biopsy samples were then processed and paraffin sections were prepared, stained, and evaluated to confirm the clinical diagnosis.

Statistical Analysis. The statistical relation between OSCC and normal, OSF and normal, and OSCC and OSF tissue data in terms of level of significance was evaluated using nonparametric Kruskal–Wallis test. Further, an additional test was performed on the same dataset using two-way ANOVA to corroborate the level of significance obtained from Kruskal–Wallis test. In all tests, $P <$ 0.05 was considered to be a statistically significant difference between the datasets. Prior to nonparametric analysis, the normality of selected data was checked using the Lilliefors test. However, the normal distribution was not found in any dataset. For the time-series data, unit root test was performed using the augmented Dickey–Fuller method with an autoregression model and the test statistics P value was determined using standard t test.

1. A. Srivastava, P. Laidler, L. E. Hughes, J. Woodcock, E. J. Shedden, Neovascularization in human cutaneous melanoma: A quantitative morphological and Doppler ultrasound study. *Eur. J. Cancer Clin. Oncol.* **22**, 1205–1209 (1986).
2. D. A. Mankoff et al., Blood flow and metabolism in locally advanced breast cancer: Relationship to response to therapy. *J. Nucl. Med.* **43**, 500–509 (2002).
3. A. Cerussi et al., Predicting response to breast cancer neoadjuvant chemotherapy using diffuse optical spectroscopy. *Proc. Natl. Acad. Sci. U.S.A.* **104**, 4014–4019 (2007).
4. M. Yang et al., Dual-color fluorescence imaging distinguishes tumor cells from induced host angiogenic vessels and stromal cells. *Proc. Natl. Acad. Sci. U.S.A.* **100**, 14259–14262 (2003).
5. H. Anderson, P. Price, M. Blomley, M. O. Leach, P. Workman; Cancer Research Campaign PK/PD Technologies Advisory Committee, Measuring changes in human tumour vasculature in response to therapy using functional imaging techniques. *Br. J. Cancer* **85**, 1085–1093 (2001).
6. N. Charkoudian, Skin blood flow in adult human thermoregulation: How it works, when it does not, and why. *Mayo Clin. Proc.* **78**, 603–612 (2003).
7. M. A. Redd et al., Patterned human microvascular grafts enable rapid vascularization and increase perfusion in infarcted rat hearts. *Nat. Commun.* **10**, 584 (2019).
8. G. Han, R. Ceilley, Chronic wound healing: A review of current management and treatments. *Adv. Ther.* **34**, 599–610 (2017).
9. A. J. Holland, H. C. Martin, D. T. Cass, Laser Doppler imaging prediction of burn wound outcome in children. *Burns* **28**, 11–17 (2002).
10. Dachun Xu et al., Sensitivity and specificity of the ankle—Brachial index to diagnose peripheral artery disease: A structured review. *Vasc. Med.* **15**, 361–369 (2010).
11. N. Ahmadi et al., Low fingertip temperature rebound measured by digital thermal monitoring strongly correlates with the presence and extent of coronary artery disease diagnosed by 64-slice multi-detector computed tomography. *Int. J. Cardiovasc. Imaging* **25**, 725–738 (2009).
12. P. Vaupel, F. Kallinowski, P. Okunieff, Blood flow, oxygen and nutrient supply, and metabolic microenvironment of human tumors: A review. *Cancer Res.* **49**, 6449–6465 (1989).
13. P. W. Vaupel, D. K. Kelleher, Pathophysiological and vascular characteristics of tumours and their importance for hyperthermia: Heterogeneity is the key issue. *Int. J. Hyperthermia* **26**, 211–223 (2010).
14. R. K. Jain, Normalizing tumor microenvironment to treat cancer: Bench to bedside to biomarkers. *J. Clin. Oncol.* **31**, 2205–2218 (2013).
15. A. Y. Rwei et al., A wireless, skin-interfaced biosensor for cerebral hemodynamic monitoring in pediatric care. *Proc. Natl. Acad. Sci. U.S.A.* **117**, 31674–31684 (2020).
16. B. A. Moffat et al., Functional diffusion map: A noninvasive MRI biomarker for early stratification of clinical brain tumor response. *Proc. Natl. Acad. Sci. U.S.A.* **102**, 5524–5529 (2005).
17. I. D. Swain, L. J. Grant, Methods of measuring skin blood flow. *Phys. Med. Biol.* **34**, 151–175 (1989).
18. D. M. McDonald, P. L. Choyke, Imaging of angiogenesis: From microscope to clinic. *Nat. Med.* **9**, 713–725 (2003).
19. M. J. Suter et al., Intravascular optical imaging technology for investigating the coronary artery. *JACC Cardiovasc. Imaging* **4**, 1022–1039 (2011).
20. G. J. Ughi et al., A neurovascular high-frequency optical coherence tomography system enables in situ cerebrovascular volumetric microscopy. *Nat. Commun.* **11**, 3851 (2020).
21. V. J. Srinivasan et al., OCT methods for capillary velocimetry. *Biomed. Opt. Express* **3**, 612–629 (2012).
22. F. E. Robles, C. Wilson, G. Grant, A. Wax, Molecular imaging true-colour spectroscopic optical coherence tomography. *Nat. Photonics* **5**, 744–747 (2011).
23. B. Ghosh et al., Quantitative in situ imaging and grading of oral precancer with attenuation corrected-optical coherence tomography. *Oral Oncol.* **117**, 105216 (2021).
24. B. Ghosh, M. Mandal, P. Mitra, J. Chatterjee, Attenuation corrected-optical coherence tomography for quantitative assessment of skin wound healing and scar morphology. *J. Biophotonics* **14**, e202000357 (2021).
25. E. R. Kaso, B. H. Annex, "Imaging needs for development of novel therapeutics in PAD" in *Imaging in Peripheral Arterial Disease: Clinical and Research Applications*, C. M. Kramer, Ed. (Springer International Publishing, Cham, Switzerland, 2020), pp. 123–145.
26. A. K. Murray, A. L. Herrick, T. A. King, Laser Doppler imaging: A developing technique for application in the rheumatic diseases. *Rheumatology (Oxford)* **43**, 1210–1218 (2004).
27. B. Ruaro et al., Monitoring the microcirculation in the diagnosis and follow-up of systemic sclerosis patients: Focus on pulmonary and peripheral vascular manifestations. *Microcirculation* **27**, e12647 (2020).
28. D. J. Newton, F. Khan, J. J. Belch, M. R. Mitchell, G. P. Leese, Blood flow changes in diabetic foot ulcers treated with dermal replacement therapy. *J. Foot Ankle Surg.* **41**, 233–237 (2002).
29. G. Varetto et al., Oxygen delivery therapy with EPIFLO reduces wound hyperperfusion in patients with chronic leg ulcers: A laser speckle contrast analysis. *Ann. Vasc. Surg.* **64**, 246–252 (2020).
30. S. M. Daly, M. J. Leahy, 'Go with the flow': A review of methods and advancements in blood flow imaging. *J. Biophotonics* **6**, 217–255 (2013).
31. A. L. Shada et al., Infrared thermography of cutaneous melanoma metastases. *J. Surg. Res.* **182**, e9–e14 (2013).
32. A. Bhowmik, R. Repaka, R. Mulaveesala, S. C. Mishra, Suitability of frequency modulated thermal wave imaging for skin cancer detection—A theoretical prediction. *J. Therm. Biol.* **51**, 65–82 (2015).
33. A. J. Guidi, S. J. Schnitt, Angiogenesis in preinvasive lesions of the breast. *Breast J.* **2**, 364–369 (1996).
34. F. Dong et al., Detection of cervical lymph node metastasis from oral cavity cancer using a non-radiating, noninvasive digital infrared thermal imaging system. *Sci. Rep.* **8**, 7219 (2018).
35. C. B. Soffin, D. R. Morse, S. Seltzer, M. S. Lapayowker, Thermography and oral inflammatory conditions. *Oral Surg. Oral Med. Oral Pathol.* **56**, 256–262 (1983).
36. B. A. White, P. B. Lockhart, S. F. Connolly, S. T. Sonis, The use of infrared thermography in the evaluation of oral lesions. *J. Am. Dent. Assoc.* **113**, 783–786 (1986).
37. A. A. Sagaidachnyi, A. V. Fomin, D. A. Usanov, A. V. Skripal, Thermography-based blood flow imaging in human skin of the hands and feet: A spectral filtering approach. *Physiol. Meas.* **38**, 272–288 (2017).
38. L. Gao et al., Epidermal photonic devices for quantitative imaging of temperature and thermal transport characteristics of the skin. *Nat. Commun.* **5**, 4938 (2014).
39. D. B. Rodrigues et al., Design and optimization of an ultra wideband and compact microwave antenna for radiometric monitoring of brain temperature. *IEEE Trans. Biomed. Eng.* **61**, 2154–2160 (2014).
40. E. S. Ebbini, "Ultrasound thermography: Principles, methods, and experimental results" in *Theory and Applications of Heat Transfer in Humans*, D. Shrivastava, Ed. (John Wiley & Sons Ltd, Chichester, UK, 2018), **vol. 1**, pp. 301–332.
41. F. Fani, E. Schena, P. Saccomandi, S. Silvestri, CT-based thermometry: An overview. *Int. J. Hyperthermia* **30**, 219–227 (2014).
42. S. Dehkharghani, D. Qiu, MR thermometry in cerebrovascular disease: Physiologic basis, hemodynamic dependence, and a new frontier in stroke imaging. *AJNR Am. J. Neuroradiol.* **41**, 555–565 (2020).
43. S. A. Tekade et al., Early stage oral submucous fibrosis is characterized by increased vascularity as opposed to advanced stages. *J. Clin. Diagn. Res.* **11**, ZC92–ZC96 (2017).
44. S. Pazouki et al., The association between tumour progression and vascularity in the oral mucosa. *J. Pathol.* **183**, 39–43 (1997).
45. X. Song et al., Oral squamous cell carcinoma diagnosed from saliva metabolic profiling. *Proc. Natl. Acad. Sci. U.S.A.* **117**, 16167–16173 (2020).
46. American Cancer Society, Cancer facts & figures 2019. https://www.cancer.org/research/cancer-facts-statistics/all-cancer-facts-figures/cancer-facts-figures-2019.html. Accessed 23 January 2020.
47. H. H. Pennes, Analysis of tissue and arterial blood temperatures in the resting human forearm. *J. Appl. Physiol.* **1**, 93–122 (1948).
48. B. Suhm, Heart sound classifier. https://www.mathworks.com/matlabcentral/fileexchange/65286-heart-sound-classifier. Accessed 20 November 2019.
49. K. S. Lee et al., Three-dimensional imaging of normal skin and nonmelanoma skin cancer with cellular resolution using Gabor domain optical coherence microscopy. *J. Biomed. Opt.* **17**, 126006 (2012).
50. A. Bhowmik et al., Measured temperature, blood perfusion, metabolic heat generation and thermal conductivity of healthy oral mucosa, OSCC and OSF. GitHub. https://github.com/Arka-Bhowmik/oral_properties. Deposited 29 May 2020.

12 of 12 | PNAS
https://doi.org/10.1073/pnas.2026201119

Bhowmik et al.
Portable, handheld, and affordable blood perfusion imager for screening of subsurface cancer in resource-limited settings